Chapter 3

The Low Temperature Phase Transition of 2,9-Decanedione/Urea

The investigation of phase transitions occupies a central portion of the study of ferroic materials.[1,2] In fact, because ferroic behavior requires a phase of reduced symmetry,[3] a transition to a phase of higher symmetry might be expected unless it is preceded by decomposition. In general, there are two varieties of phase transitions. *Ferroic* phase transitions involve the onset of or change in a ferroic property; for instance, crystals of Y-Ba-Cu-O exhibit ferroelastic twinning[4] on cooling to 675-1050 K[5,6] (here, the variability of transition temperature depends on sample history), whereas α-quartz undergoes a pressure-induced ferroic transition between 21 and 22 GPa.[7] Rochelle Salt, the first known ferroelectric,[8] exhibits two temperature-induced ferroic transitions, one at 18° and the other at -24 °C.[9,10] (In the temperature range between these transitions, the crystal is both ferroelectric and ferroelastic.[11]) Many of the UICs discussed in this thesis undergo ferroic phase transitions. Less relevant to the discussion are *nonferroic* phase transitions; these involve simply a change in the translational symmetry in the crystal.[12] For example, octafluoronaphthalene undergoes a doubling of the crystallographic *a*-axis when cooled to 266 K, yet it retains its $P2_1/c$ space symmetry throughout the phase transition.[13]

Ferroic phase transitions can be divided into two classes. Those that involve a change in point symmetry are known as *ferroelastic* phase transitions, while those that do not are called *nonferroelastic*.[2] The present discussion is solely concerned with ferroelastic phase transitions. As a crystal undergoes a ferroelastic phase transition, the emergence of strain can accompany the change from high temperature to low temperature

phase. However, it is not always true that the high temperature phase can be attained. Indeed, melting or decomposition may precede this event.

In the late 1960s, the physicist Aizu developed a theory of ferroics that includes a derivation of the varieties of possible ferromagnetics, ferroelectrics, ferroelastics and mixtures thereof.[14] He realized that each of the ferroic point groups could be thought of as possessing a minor distortion from some phase of greater symmetry. This higher symmetry state is known as the *prototype*. The *prototypic* phase[15] includes the symmetry elements of the ferroic phase (and others), yet its high symmetry prevents it from possessing ferroic properties; instead, it is paraelectric, paraelastic, *etc*. Because the symmetry of the ferroic phase is a subset of the symmetry of its prototype, the transition from the prototypic phase to the ferroic phase necessarily involves the loss of one or more symmetry elements. Since it involves a change in point symmetry, the transition from the prototypic phase to the ferroic phase is ferroelastic, even if the ferroic phase possesses no ferroelastic distortion.

The interconversion between different orientation states of the ferroic phase is a requisite property of ferroic behavior. However, it is possible for a crystal to have two ferroic phases whose orientation states are not interconvertible. An example of this is illustrated in Figure 3.1. In the figure, a hypothetical 2-D ferroelastic crystal is shown to have at least two sets of orientation states that are not interchangeable. For this reason, Aizu[14] derived ferroic *species* that are assigned based on the symmetry of the prototypic and ferroic phases and the symmetry relationships between them. For example, the prototype (**1**, in Figure 3.1) has point symmetry 4/mmm. (This assignment assumes a mirror plane in the page.) It is highly symmetric and has no in-plane distortion from

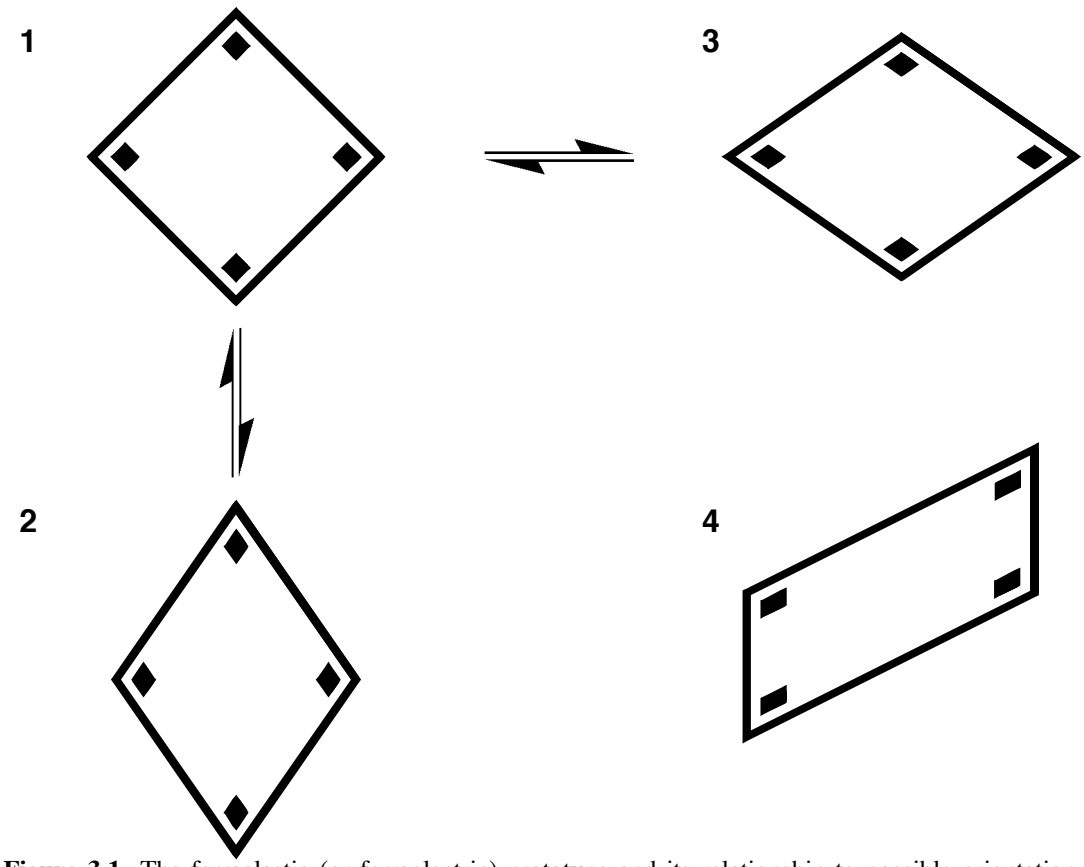

Figure 3.1 The ferroelastic (or ferroelectric) prototype and its relationship to possible orientation states. According to Aizu, a ferroic orientation state exhibits a small deviation from a nonferroic phase with higher symmetry. Here, a potentially ferroelastic phase is depicted (in two dimensions) as a parallelogram (**2**). This parallelogram exhibits a minor distortion from a phase of higher symmetry (**1**). The high-symmetry rectangle, **1**, possesses no strain and therefore cannot be ferroelastic. Because a minor distortion of **1** leads to the ferroelastic **2**, phase **1** is paraelastic and possesses the prototype symmetry of **2**. The phase transition between **1** and **2** involves a change in point group and is therefore said to be *ferroelastic* (see text). The corners have been labeled to illustrate the position and orientation of the object (or unit cell), which are not altered during the phase transition. For **2** to be functionally ferroelastic, there must be at least one additional orientation state accessible from the same prototype. The obvious choice is **3**. By applying force in the appropriate direction it is possible to interconvert **2** and **3**. Orientation states **2** and **3** share all properties except the orientation of ferroelastic distortion. It is commonly held that transitions between orientation states occur via a prototypic intermediate (or transition state), so the arrows between states have been drawn accordingly. There are other possible ferroelastic states derivable from **1**, an example being **4**. Although this phase shares **1** as a prototype, it is not attainable directly from either **2** or **3** and is therefore not an orientation state of **2** and **3**. Instead, the ferroelastic phase transition connecting **1** and **4** comprises a different *species* of phase transition (refer to text). By exchanging the concept of "ferroelastic distortion" with "dipole moment," this figure describes ferroelectric transitions, as well. The table below lists the 16 point groups capable of ferroelasticity and the ten point groups capable of ferroelectricity. Those groups marked with (*) are potentially ferroelastic and ferroelectric. See text for additional details.

ferroelastic point groups		**ferroelectric point groups**	
1*	3*	1*	4mm
$\bar{1}$	$\bar{3}$	2*	3*
2*	422	m*	3m*
m*	32	mm2*	6
2/m	$\bar{4}$2m	4	6mm
222	3m*		
mm2*	4/mmm		
mmm	$\bar{3}$m		

another symmetry; it can therefore be prototypic to other phases. The phase transition from 4/mmm to mmm, which is denoted 4/mmmFmmm in Aizu's nomenclature, involves a change in point group and is therefore a ferroelastic transition. (In this nomenclature, the F denotes a ferroic phase transition.) Two possible diagrams with mmm symmetry, **2** and **3**, are depicted in the figure. These are obviously distorted forms of the prototype, possess a strain (or moment), and are simply different orientation states of the same phase. If one can reorient the strain (or moment) from **2** to **3**, this material will be ferroic.

However, Figure 3.1 illustrates another distorted phase, **4**. This structure, of point symmetry 2/m, again exhibits a distortion from the prototype symmetry so that it is also potentially ferroic. However, this phase contains orientation states in common with neither **2** nor **3**, so it should exhibit different physical properties. Because they belong to different species, the orientation states of **2**(**3**) and **4** are not interconvertible by a domain switching process. Thus, the species 4/mmmFmmm is a ferroelastic phase that must be distinguished from the species 4/mmmF2/m and other ferroelastic phases that share the same prototype. With this in mind, Aizu derived 88 species of ferroelectrics that include ten of the 32 crystallographic point groups. Furthermore, 94 ferroelastic species are derived from 16 point groups; 42 of these are also ferroelectric.[14,16,17] The point groups capable of ferroelastic or ferroelectric behavior (or both) are listed in the table in Figure 3.1. In total, there are six crystallographic point groups that are potentially ferroelectric and ferroelastic. These are 1, 2, m, mm2, 3 and 3m.

Phase transitions in urea inclusion compounds have been studied extensively.[18] When UICs are heated above room temperature, there is a general consensus that increased rotational freedom[19,20] precedes decomplexation[21,22] and that decomplexation of

low melting guests generates tetragonal urea, which crystallizes and then melts at a higher temperature.[23] However, many investigations have centered on low temperature phase transitions,[19,24-29] in which UICs of *n*-alkanes undergo a change from hexagonal to lower symmetry. Experiments have shown this transition to depend on the guest chain length,[30,31] and host-guest interactions are thought to dominate the energetics of phase transition behavior.[32]

When viewed along their longest axis, the polymethylene chain of opposing CH_2 groups makes saturated hydrocarbons appear rectangular in shape. This mirror symmetry is not compatible with the sixfold symmetry of the urea channel, but at ambient temperatures, it is thought that rotational averaging makes the time- and space-averaged structures of most alkane UICs hexagonal. (However, an important caveat is that hexadecane/urea is optically biaxial and therefore not truly hexagonal at room temperature.[33]) In a low temperature regime, however, decreased rotational motion can give rise to long-range ordering of guests. Based on the temperature dependence of diffuse X-ray scattering by *n*-tetracosane guest,[34,35] rotational correlations between guests in neighboring channels were shown to change anomalously near the phase transition temperature. Although their longitudinal mean-squared displacements are temperature dependent, the longitudinal correlation lengths of *displacements* between guests within the same channel and in adjacent channels are relatively insensitive to temperature.[35] Thus, rotational guest motions[36] and disorder[25,26] are intimately linked to phase transition behavior in alkane/UICs. As the guests lose rotational freedom, the channel may distort[24,25,37] to accommodate the chains, and intrachannel orientational ordering results.[28] In cases where it has been measured, the symmetry of the low temperature phase is

usually orthorhombic (for example, *n*-hexadecane/urea is $P2_12_12_1$[24,25]). Thus, the low temperature phase transition for *n*-hexadecane/urea is expected to be a ferroelastic phase transition of species 622F222. (The 622F222 phase transition has been inferred by certain authors in urea inclusion compounds containing certain other *n*-alkanes[29] and dicarboxylic acids.[38])

Consistent with these findings is the demonstration of ferroelasticity in UICs containing linear alkanes,[29] α,ω-dicarboxylic acids[29,38,39] and alkanediones.[40] For many ferroelastic UICs, the application of compressive stress results in a domain switching event not unlike that observed for 2,10-undecanedione/urea (discussed in Section 1.1.2): a ~60° reorientation of the strain that accommodates the applied force. For ferroelastics such as these, there are three degenerate orientation states, as predicted by Aizu for the 622F222 species.[14]

In this chapter, the study of structural phase transitions in 2,9-decanedione/urea will be discussed. These phase transitions are similar to phase transitions exhibited by alkane UICs[19,25] because they all involve changes in symmetry. The implications for ferroelastic behavior in this UIC makes an understanding of the phase transitions in 2,9-decanedione/urea significant to the study of ferroelasticity in urea inclusion compounds.

3.1 Survey of the Phase Transition

At room temperature, the crystal structure of 2,9-decanedione/urea is commensurate[41] with $3c_g' = 4c_h'$. (Refer to Section 1.1.2 and Figure 1.5.) Within each unit cell, the guest molecules are related by a threefold screw along the channel axis. The space group symmetry for this structure is $P3_112$ or the enantiomorphic $P3_212$. Because

certain ureas are crystallographically inequivalent, there are very minor positional displacements of the host molecules from an idealized hexagonal structure; however, the trigonal rotational symmetry along this axis results in the overall cancellation of these displacements. For this crystal, reduction from trigonal rotational symmetry (induced, perhaps, by cooling), could potentially lead to the onset of ferroelastic distortion.

3.1.1 Differential Scanning Calorimetry

To test the effects of cooling, differential scanning calorimetry (DSC) was performed on UICs containing 2,9-decanedione for temperatures between room temperature and -180 °C. When cooled at 10 °C min^{-1}, a sample of 2,9-decanedione/urea exhibited no thermal anomalies until approximately -167 °C (Figure 3.2). At this temperature, an exothermic peak is observed with an onset temperature (T_{onset}) of -167.2 °C. Upon warming, a complimentary endotherm is observed with T_{onset} = -167.8 °C. Closer inspection of both cooling and heating curves shows that there are actually two peaks (Figure 3.2b); however, they are not well resolved. The observation of the same peaks in the heating and cooling curves indicates a set of reversible phase transitions that are responsible for the thermal anomalies.

Although these phase transitions have been observed by DSC for several different samples, accurate determination of the transition enthalpies (ΔH) has been difficult. For instance, in Figure 3.2, the combined enthalpy (on cooling) for both anomalies is -0.532 kcal $(\text{mole guest})^{-1}$; for the warming transition, ΔH = 0.128 kcal $(\text{mole guest})^{-1}$. Such a large discrepancy in measured values may artificially arise from the rate of cooling and heating (10 °C min^{-1}). This assumption was confirmed by running the DSCs at a

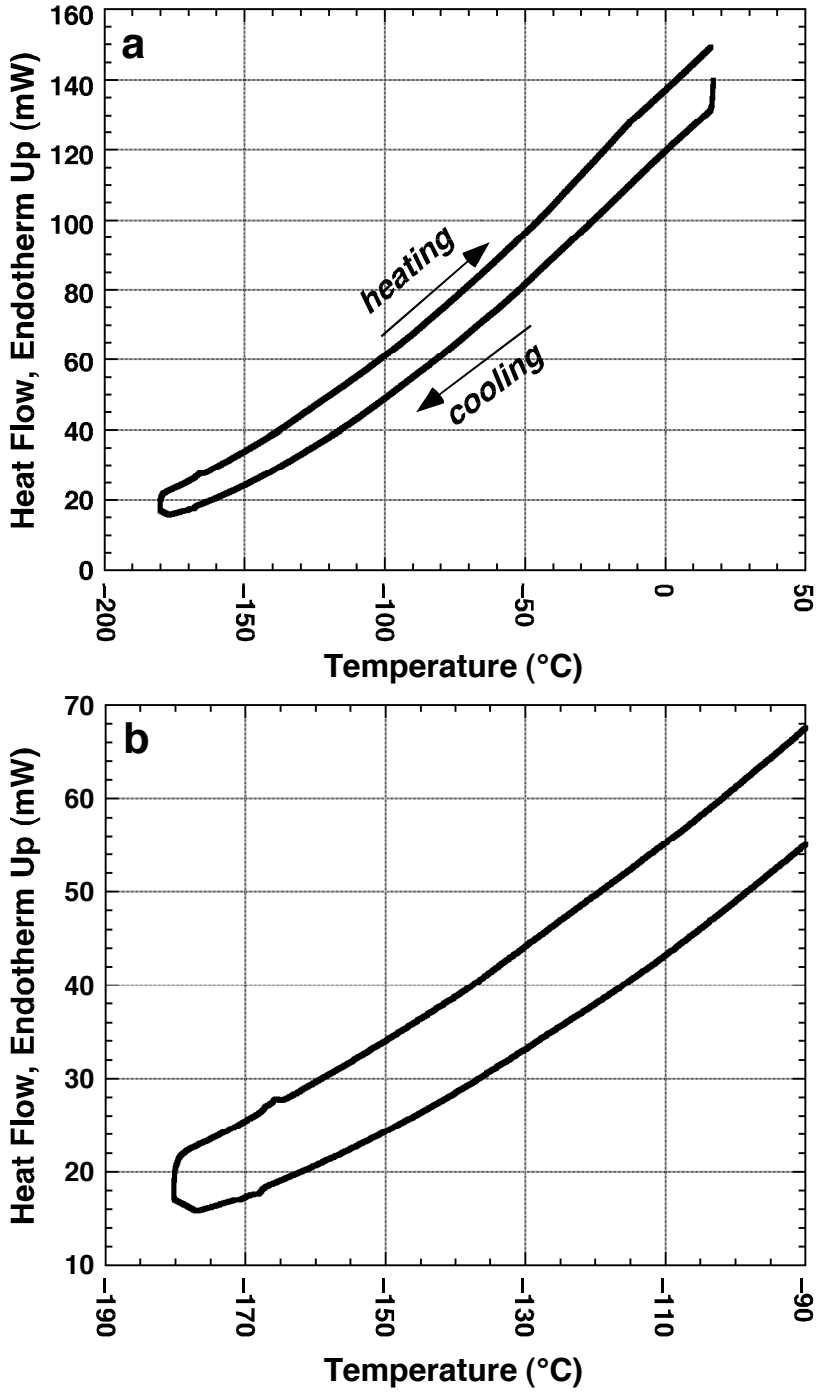

Figure 3.2 Differential scanning calorimetry (DSC) of 2,9-decanedione/urea. Here, 28.05 mg of lightly crushed crystals were cooled, then heated at a rate ($\Delta T/\Delta t$) of 10 °C min^{-1}. **(a)** Between room temperature and –165 °C the trace appears featureless (the broad peak centered at –10 °C is an artefact of the instrument). **(b)** A close-up image of the same DSC run. Near –165 to –170 °C, thermal anomalies are observed in the cooling and heating curves; these represent phase transitions within the sample. On cooling, the onset temperature (T_{onset}) is observed at –167.2 °C, with transition enthalpy (ΔH) = –0.532 kcal (mole guest)$^{-1}$. Upon heating, T_{onset} = –167.8 °C and ΔH = 0.128 kcal (mole guest)$^{-1}$.

cooling/heating rate of 5 °C min^{-1} (Figure 3.3). Here, a sample of 2,9-decanedione/urea provides two thermal anomalies that are clearly distinguishable; for both anomalies, the transition enthalpies recorded for two separate cycles of cooling and heating are comparable. In **a**, the sample was cooled from -148 °C to -182 °C and then heated. Upon cooling, two anomalies were observed between -170.5 and -173.5 °C. As the sample was warmed through this temperature range, the reverse transition occurred between -171.0 and -168.7 °C. Because both species are in equilibrium at the phase transition, the free energy change, ΔG, is zero. Using the Gibbs equation, the phase transition enthalpy can therefore be calculated using the transition temperature and the transition enthalpy. For this sample, ΔH = -0.407 kcal (mole guest)$^{-1}$ and ΔS = -3.96 cal (mole guest K)$^{-1}$ during the cooling cycle; upon warming, ΔH = 0.483 kcal (mole guest)$^{-1}$ and ΔS = 4.73 cal (mole guest K)$^{-1}$. A repeat run of the same sample through an identical thermal cycle produced similar results (Figure 3.3c-d).

Overlap of the pair of endothermic events made independent integration of these impractical for the heating curve; however, separation in the (5 °C min^{-1}) cooling curve was adequate for the determination of the transition enthalpies for each event. By measuring each exotherm separately, it was demonstrated[42] that the ratio of enthalpies for first (higher temperature) to the second (lower temperature) peak is 0.98(7) for the pair of experiments described in Figure 3.3. (Here, the ratio of the first peak to the second peak was 1.03:1 for the first run (Figure 3.3a-b) and 0.93:1 for the second run (Figure 3.3c-d).) Thus, it can be concluded that each transition contributes roughly half of the total enthalpy, or that each transition is worth approximately 0.20 to 0.25 kcal (mole guest)$^{-1}$. This value is on the order of those found for the rotational order-disorder transitions for

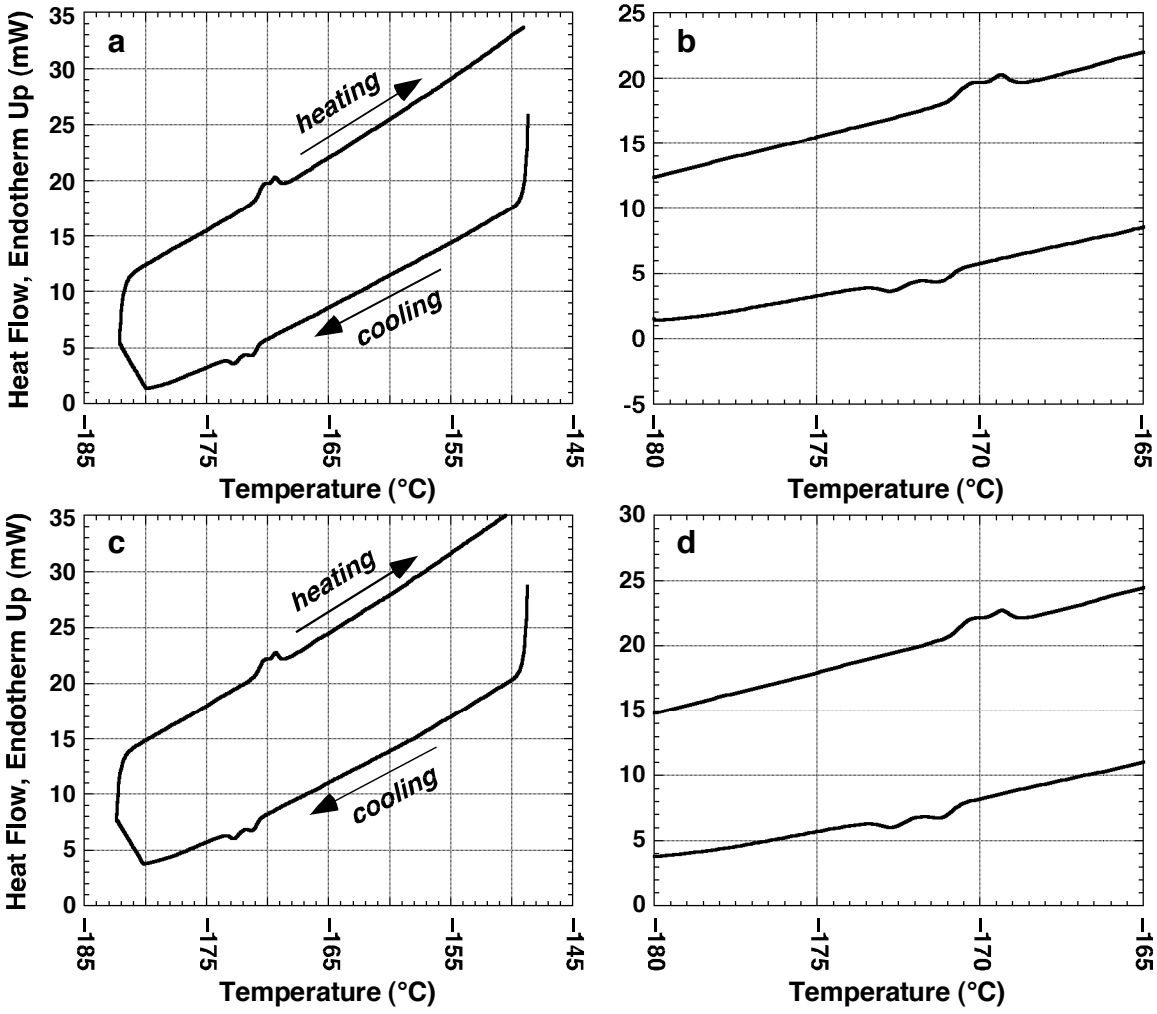

Figure 3.3 The low-temperature phase transition in 2,9-decanedione/urea observed with differential scanning calorimetry (DSC). Here, 34.75 mg of lightly crushed crystals of 2,9-decanedione/urea were cooled and then warmed at a rate ($\Delta T/\Delta t$) of 5 °C min^{-1}. **(a,b)** The first DSC cycle. While cooling from –148 °C, T_{onset} for an exothermic transition was –170.5 °C, with ΔH = –0.407 kcal (mole guest)$^{-1}$ and ΔS = –3.96 cal (mole guest K)$^{-1}$. Upon heating, the endothermic transition had T_{onset} = –171.0 °C, ΔH = 0.483 kcal (mole guest)$^{-1}$ and ΔS = 4.73 cal (mole guest K)$^{-1}$. This transition contains two thermal events, with T_{onsets} of approximately –170.5° and –172.1 °C, (for the cooling curve). **(c,d)** The second DSC cycle, performed with the same sample immediately following the first run. On cooling, T_{onset} = –170.5 °C, ΔH = –0.389 kcal (mole guest)$^{-1}$ and ΔS = –3.79 cal (mole guest K)$^{-1}$. Upon heating, T_{onset} = –171.0 °C and ΔH = 0.473 kcal (mole guest)$^{-1}$ and ΔS = 4.63 cal (mole guest K)$^{-1}$. For this run, the pair of events occurred at T_{onsets} of approximately –170.5 and –171.8° C. Although they were not completely resolvable (even for slow ΔT), the area of the thermal events is roughly equivalent: for the two runs, their ratio is 0.98 (0.07). Other DSC experiments (see Figure 3.2) indicate no additional thermal anomalies between –180 °C and 20 °C.

alkane-UICs;[31,43] however, UICs containing alkanes are very different from 2,9-decanedione/urea so that this similarity is likely coincidental. Similarly, ΔS for each transition is approximately 2.0-2.3 cal (mole guest K)$^{-1}$. Using classical thermodynamics, one can relate the entropy change to the degrees of freedom lost (or gained) upon cooling (or warming) through the phase transition via the equation $\Delta S = R\ln(w)$. Here, w is the degrees of freedom and R is the ideal gas constant (1.987 cal mole^{-1} K^{-1}). For ΔS ~ 2.2 cal (mole guest K)$^{-1}$, w = 3; given the current understanding of this transition and the many possible events it might entail, it is difficult to provide a physical description of the meaning of w.

3.1.2 X-Ray Diffractometry

What is the nature of this transition, and what physical processes can be tied to the two thermal events described in Figure 3.3? These questions were addressed using single crystal X-ray oscillation diffractometry, which has been applied to other urea inclusion compounds.[44-46] The experiments were performed by Mark D. Hollingsworth with collaborators Bertrand Toudic and Philippe Rabiller at the Université de Rennes, France. In this experiment the crystal is mounted and carefully aligned so that it can be rotated about its channel axis, which is perpendicular to the X-ray beam.

Figure 3.4a presents an oscillation image of 2,9-decanedione/urea, collected at room temperature. In this crystal the host channel and guest molecules exhibit 11.0 and 14.7 Å spacings along the channel axis, respectively,[41] which makes their layer lines discernible.[45] The 11.0 and 14.7 Å^{-1} reciprocal lengths of the host and guest substructures, respectively, are observed along c^*. Along this direction, every third layer

line from the center (e.g., (hk3), (hk6), etc.) corresponds to some fraction of the 14.7 $Å^{-1}$ repeat; although every reflection has contributions from each substructure, the intensity of these layer lines is thought to be dominated by the guest substructure.[45] These reflections are therefore labeled $(hk1)_g$, $(hk2)_g$, etc., according to the convention of Harris and Thomas;[45] in Figure 3.4a, they are denoted using "g". In a similar fashion, every fourth layer line from the center corresponds to some fraction of the 11.0 $Å^{-1}$ repeat of the urea helix. For these, reflection intensity is dominated by the host repeat so the reflections are denoted $(hk1)_h$, $(hk2)_h$, etc; in Figure 3.4a, they are denoted using "h". (By this convention, every twelfth layer line should have significant intensity contributions from both host and guest substructures, as should (hk0).) The $3c_g' = 4c_h'$ commensurate relationship between host and guest sublattices ensures periodic overlap of host and guest layer lines (see Section 1.1.2 for a discussion). In Figure 3.4a, reflections arising from the commensurate repeat exhibit the closest spacing, 44.16 $Å^{-1}$. (One of these is circled).

By recording oscillation images at temperatures above, below, and at the phase transitions, it is possible to assess the events occurring during these phase transitions in 2,9-decanedione/urea. In this study, oscillation images were recorded between room temperature and -183 °C. At higher temperatures, a single set of reflections is observed. In each image the crystal is positioned with its *c* (channel) axis along the horizontal so that reflections from *c** are spaced from right to left, while indices in *a***b** are displaced vertically. In the room temperature image, Figure 3.4a, the spacing of reflections corresponds to the trigonal 8.229 × 8.229 × 44.16 Å cell observed in 2,9-decanedione/urea.[41] A data set that consisted of 60 six degree (in ϕ) rotation frames was

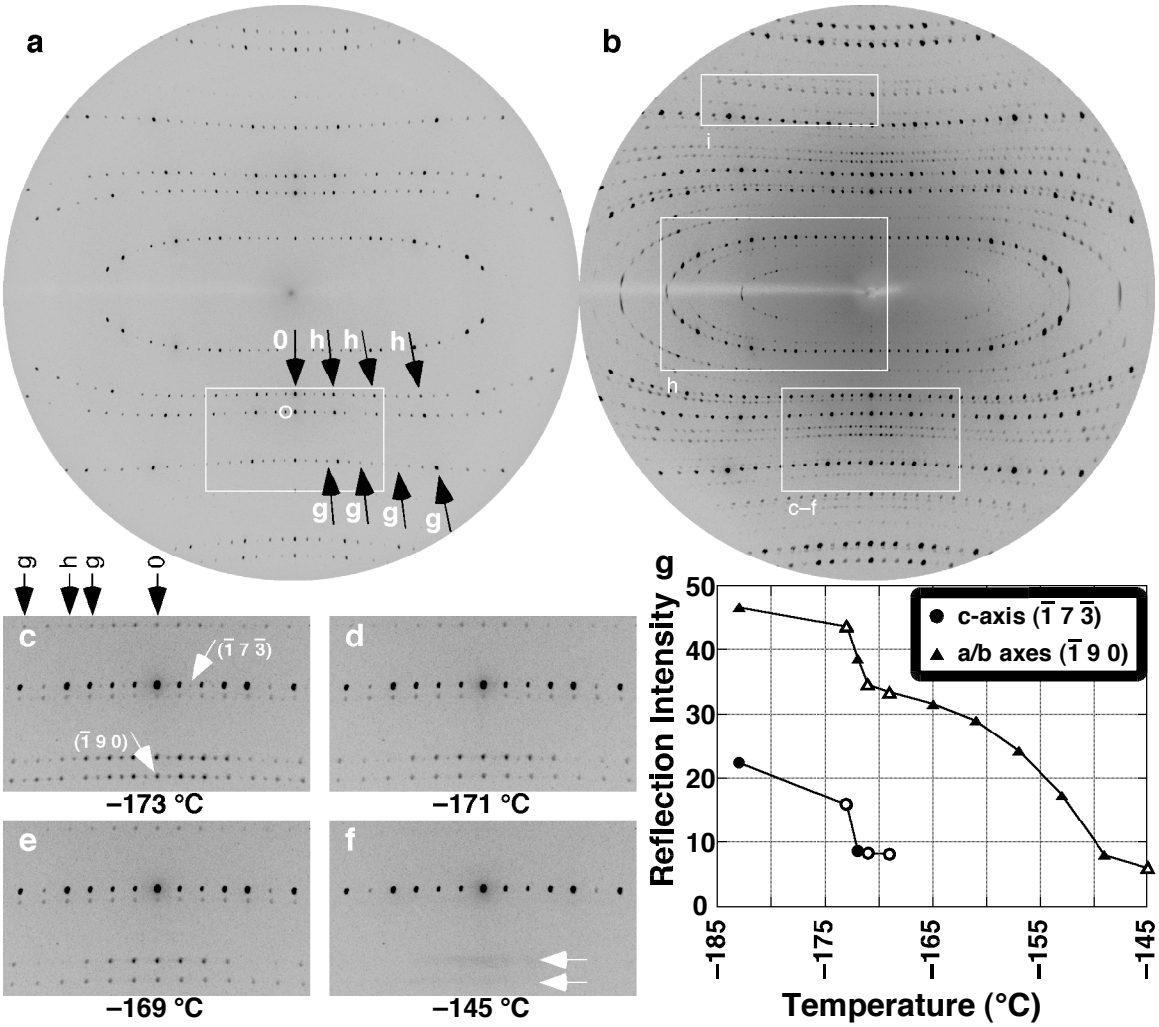

Figure 3.4 The low temperature phase transition in 2,9-decanedione/urea as observed by X-ray channel-axis oscillation photography. **(a)** A rotation image collected at room temperature. Here, reflections in c* are spaced horizontally; reflections in a*b* are spaced vertically. Host layer lines (labeled h) along c* consist of discrete spots of 11.0 $Å^{-1}$ spacing. Guest layer lines (labeled g) along c* have 14.7 $Å^{-1}$ spacing. Coincidence of the third host layer line $(hk3)_h$ and the fourth guest layer line $(hk4)_g$ demonstrate that this crystal is commensurate ($3c_g' = 4c_h'$) with a 44.16 Å channel axis repeat length. Upon cooling, additional reflections emerge along a*b* and c*. In **b**, the crystal has been cooled to –183 °C; here, additional reflections are apparent. **(c-f)** By measuring the intensity of the additional reflections at various temperatures (open symbols in **g**) it is possible to monitor two phase transitions. These images are expanded views of the region outlined in **a** and **b** from images collected at –173° (**c**), –171° (**d**), –169° (**e**) and –145 °C (**f**). In **c**, the h and g layer lines observed in the room temperature image (**a**) are denoted with black arrows. At this temperature the presence of extra reflections along c* and along a*b* indicates unit cell expansion along c and in the ab plane. Upon warming to –169 °C (**e**), the 88 $Å^{-1}$ reflections have disappeared, but expansion in the ab plane persists to –145 °C (**f**). **(g)** A plot of reflection intensity for additional reflections along a*b* and c* versus temperature. Here, reflections were indexed according to the 16 x 28 x 88 Å orthorhombic cell described in the text: $(\bar{1}\ 9\ 0)$, ▲, is used to characterize expansion in the ab plane and is observed below –145° C; $(\bar{1}\ 7\ \bar{3})$, ●, characterizes expansion along the c-axis and is observed below –169 °C. Reflection intensity is plotted in arbitrary units; intensity for $(\bar{1}\ 7\ \bar{3})$ has been multiplied by a factor of three. **(h,i)** Close-up view of a portion of the –183 °C image. In **h**, reflections from each of the orthorhombic unit cells are defined. In **i**, split reflections are observable. (See text.)

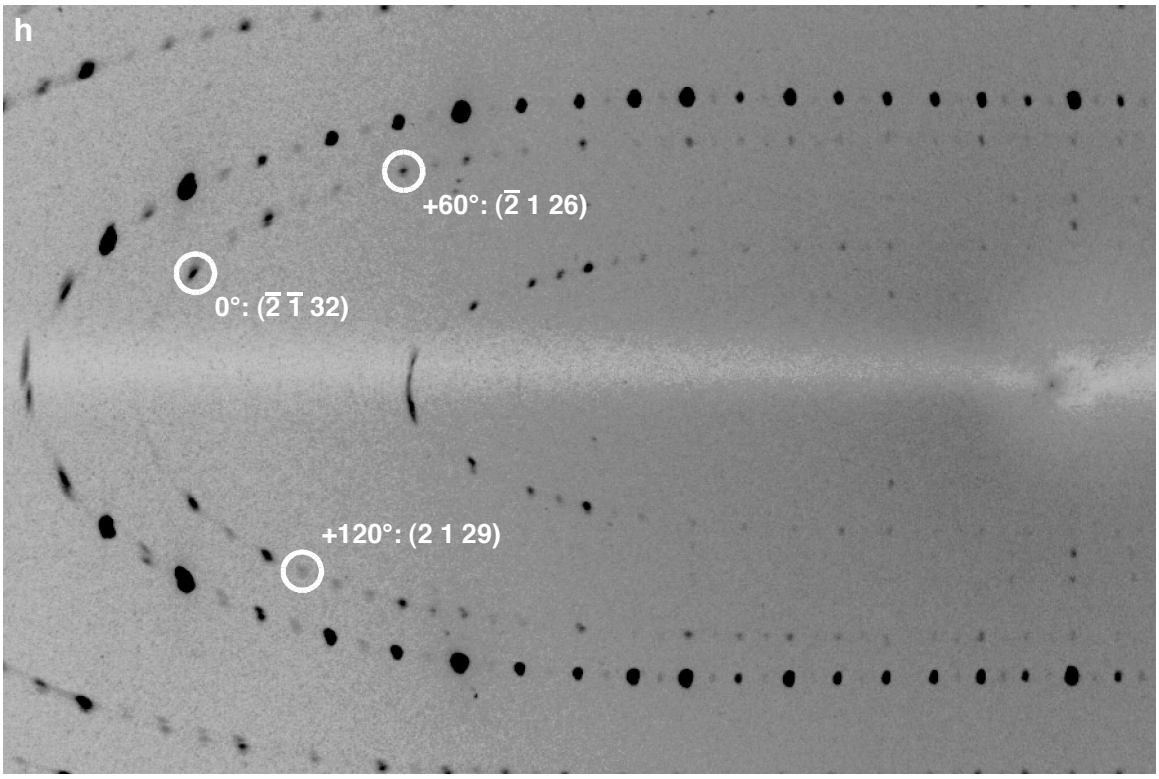
h
+60°: (2̄ 1 26)
0°: (2̄ 1̄ 32)
+120°: (2 1 29)

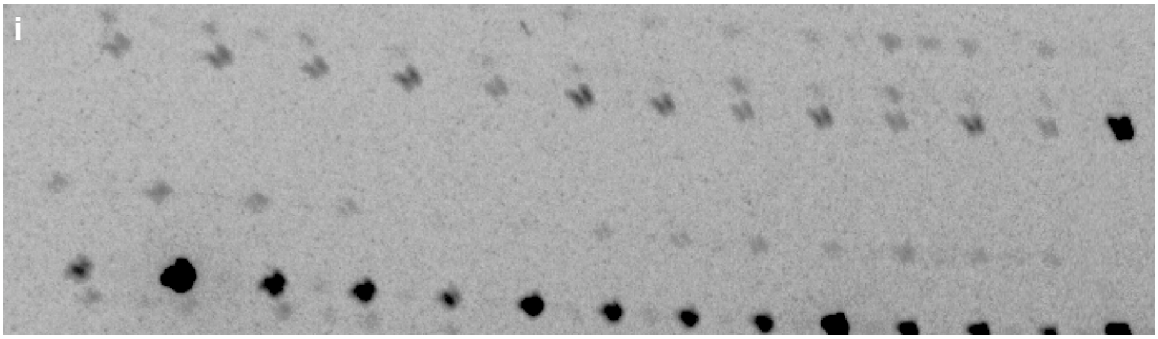
i

collected at -133 °C.[47] Using CrysAlis Red (v. 1.171.24 beta, for Windows), 485 reflections were refined[48] (using no constraints) to provide the following lattice constants:

a = 8.111 (13) Å	α = 90.10 (7)°
b = 8.133 (15) Å	β = 89.95 (7)°
c = 43.836 (3) Å	γ = 120.0 (2)°.

Within the reported errors, this cell appears metrically hexagonal. These reflections were then constrained[49] to hexagonal symmetry to provide the following constants:

a = 8.1159 (9) Å
b = 8.1159 (9) Å
c = 43.836 (4) Å.

As the crystal is cooled to -183 °C, the rotation images become much more interesting (Figure 3.4b) as additional reflections appear along a^*b^* and along c^*. Because they are closer together in reciprocal space, these reflections indicate an enlargement of the unit cell. Visual inspection of the reflection positions along c^* indicates a doubling of the channel axis from 44 Å to 88 Å. Furthermore, spacing of the additional reflections along a^*b^* indicates an increased spacing in the ab plane. From the rotation images alone, one cannot discern the nature of the cell expansion in the ab plane; however, data set collection and unit cell refinement can provide this information.

Data collection, which consisted of 60 three degree (in ϕ) rotation frames, was performed[50] at -183 °C. The reflections observed initially suggested doubling of all three axes. Initial indexing[51] of thirty of the frames (to keep the number of observed reflections manageable) followed by unconstrained refinement[52] of 2729 reflections provided the following lattice parameters:

a = 16.193 (7) Å	α = 89.960 (13)°
b = 16.181 (5) Å	β = 90.068 (14)°
c = 87.489 (3) Å	γ = 120.07 (4)°.

As before, this cell appears metrically hexagonal; refinement,[53] constrained to hexagonal symmetry, provided the following unit cell:

a = 16.166 (3) Å
b = 16.166 (3) Å
c = 87.485 (11) Å.

Visual inspection[54] of the reciprocal lattice indicates many first order reflections in h and k, which preclude the assignment of a potential 8 × 16 × 88 Å lattice. However, the hexagonal metric symmetry permits indexing in an orthohexagonal setting; for an undistorted orthorhombic cell in which doubling of both a and b occurs, a = 16 Å and $b = a\sqrt{3} = 28$ Å. Although weak, reflections with reciprocal spacings of 28 Å^{-1} were observable in the original frames,[55] indicating the presence of a primitive cell with dimensions 16 × 28 × 88 Å. In Aizu's development of ferroic species,[14] there are no ferroelastic phase transitions that give rise to orthorhombic structures that can occur from a trigonal $P3_112$ prototype structure. Thus, the apparent orthorhombic metric symmetry is thought to be higher than the Laue symmetry of this low temperature phase. Nevertheless, this low temperature phase will be called the orthorhombic phase in this discussion since its unit cell parameters are orthorhombic within the limits of error.

Using Aizu's nomenclature, a likely phase transition would be to a monoclinic unit cell and would have species 32F2; this should give rise to three degenerate orientation states in the low temperature phase. (By virtue of the change in point symmetry, this phase transition is a ferroelastic phase transition; in addition, species 32F2 is potentially ferroelectric.) The presence of three corresponding unit cells complicates the process of identifying distinct low symmetry cells. However, the orthorhombic (or lower) symmetry assignment is supported by a search[56] for first order (k = 1) reflections

for the 28 Å cell. In this study, each of the three orientation states was identified by transforming the unit cell in increments of 60°. At +60° and +120° (from the initial orientation), the lattice parameters remained invariant (within error), and first order reflections in k were observable from each. For each orientation, unique reflections belonging to the family {2 1 ℓ} were identifiable in the low temperature oscillation image presented in Figure 3.4b; these are defined in Figure 3.4h. Here, ($\bar{2}$ $\bar{1}$ 32) is identified for the first orthorhombic cell (0°), ($\bar{2}$ 1 26) is identified for the cell rotated by +60°, and (2 1 29) is identified for the cell rotated by +120°. (Analogous reflections with negative ℓ indices, i.e., (2 1 $\overline{29}$), etc., were also identified;[56] these lie on the other end of the oscillation image and are not visible in this cutout region.) These observations are consistent with the growth of the unit cell along each of its axes upon cooling and with the assignment of primitive orthorhombic symmetry or lower. In any case, the presence of three orthorhombic cells is consistent with the biaxial nature and domain structures of this low temperature phase, as described below.

For three undistorted, orthorhombic domains related in increments of 60°, the reflections should overlap so that the domains are twinned by merohedry.[57,58] However, any distortion from hexagonal metric symmetry will destroy the merohedral relationship so that reflections from each cell will be independently observable at high diffraction angles. In the low temperature oscillation image (Figure 3.4b), certain high-angle reflections exhibit splitting. For clarity, a close-up view of the boxed region labeled "i" in Figure 3.4b is provided in Figure 3.4i. Here, splitting of higher order reflections is

obvious. Thus, the low-temperature phase of this crystal is composed of distorted unit cells (possessing orthorhombic or lower symmetry).

The data collected at -183 °C was transformed to a 16 × 28 Å unit cell, and refined[59] (with no lattice constraints) to produce the following cell,

a = 16.221 (6) Å	α = 89.99 (12)°
b = 28.069 (7) Å	β = 89.96 (15)°
c = 87.658 (4) Å	γ = 90.2 (3)°.

Using orthorhombic constraints, the low temperature data were refined with the following lattice parameters:[60]

a = 16.2111 (15) Å
b = 28.067 (2) Å
c = 43.831 (3) Å.

Note that this cell has the original, 44 Å, c-axis constant. Although CrysAlis would not retain them in the orthorhombic refinement, first order reflections from the 88 Å c-axis are observable so that, even though it cannot be refined as such (with orthorhombic constraints), this parameter should be:

c = 87.662 (6) Å.

Since this cell contains contributions from all three orthorhombic unit cells, it exhibits orthohexagonal lattice constants, i.e., $b = a\sqrt{3}$. Unfortunately, it was not possible to separate reflections from the overlapping domains, so quantification of distortion has not been conducted.

Following data set collection at -183 °C, the crystal was warmed to -165 °C, and rotation images were collected at -173° and -169 °C. At this point the crystal was cooled again, and rotation images were collected at -171 and -172 °C. Close-up portions of images obtained at -173, -171, -169 and -145 °C are presented in Figure 3.4c-f. Although

they were not collected in order of ascending temperature, the recurrence of the same additional reflections during recooling along a^*b^* and c^* suggests that this system behaves reversibly (see below).

To follow the progress of each transition, the intensity of a reflection from each sublattice was determined for each of the low-temperature images. Using Adobe Photoshop (v. 7.0, for the Macintosh), reflections $(\bar{1}\ 9\ 0)$ and $(\bar{1}\ 7\ \bar{3})$ (indexed[61] using the 16 × 28 × 88 Å cell) were used to measure the intensities of reflections emerging along a^*b^* and c^*, respectively.[62] These reflections, identified in Figure 3.4c, were chosen for their reliable intensity throughout the series of images. The intensity of each was corrected for any variations in frame brightness, etc., by comparing its intensity to that of immediately adjacent background region. Reflection $(\bar{1}\ 9\ 0)$ was chosen because its layer (along a^*b^*) is observed only in the low temperature phase. Although events occurring perpendicular to the channel cannot be completely resolved from those occurring along it, this reflection should be less affected by changes occurring along the channel axis than other reflections for which $l \neq 0$. (The reflections with $l = 0$ contain contributions from both 44 Å and 88 Å components, each of which is projected onto the basal plane.) By the same token, the reflection with $l \neq 2n$ $(\bar{1}\ 7\ \bar{3})$ was chosen to monitor doubling along c. Because it is in a layer line (along a^*b^*) that is present over the entire range of temperatures, the intensity of this reflection should be less affected by structural changes occurring in the ab plane.

The corrected intensities are plotted in Figure 3.4g. Here, the intensity of $(\bar{1}\ 7\ \bar{3})$ is plotted using circles, whereas the intensity of $(\bar{1}\ 9\ 0)$ is plotted using triangles. Open symbols are used at temperatures corresponding to the close-up images provided in

Figure 3.4c-f. These intensities are plotted using an arbitrary scale. Starting at -145 °C, some intensity (approximately 15% of the maximum intensity observed at -183°) is observable in the region of ($\bar{1}$ 9 0) reflection; this is easily noticed in the oscillation image as a broad, horizontal streak. (See arrows in Figure 3.4f.) Thus, the onset of interchannel ordering in the *ab* plane apparently begins above -145 °C. (This behavior is again discussed in Section 3.2.) As the temperature is lowered, reflection intensity increases substantially, although the slope appears to level off below -161° or so. With the exception of the discontinuity near -171° to -173 °C, the intensity of ($\bar{1}$ 9 0) increases fairly steadily. Near these temperatures there is an abrupt increase in intensity, which is discussed below.

For clarity, the corrected intensity of reflection ($\bar{1}$ 7 $\bar{3}$) (*c*-axis doubling) has been multiplied by a factor of three. This reflection, which is not observable above -169 °C, is quite weak compared to the 44 $Å^{-1}$ reflections. (In general, 88 $Å^{-1}$ reflections in this layer appear less intense than those emerging in other layer lines. Nevertheless, this reflection was chosen because its intensity should be less affected by the transition that occurs along *ab*.) Between -169° and -171° (Figure 3.4e and d), the intensity of this reflection is about 40% of the maximum observed (at -183 °C) and increases negligibly. (Although not apparent in the close-up image recorded at -169 °C (Figure 3.4e), this reflection is noticeable at -171 °C (Figure 3.4d).) At -173 °C (Figure 3.4c), the reflection intensity has increased substantially, and by -183 °C (Figure 3.4b), ($\bar{1}$ 7 $\bar{3}$) is quite intense and is easily observed in the oscillation images.

The data presented in Figure 3.4g suggest that, upon cooling, emergence of interchannel ordering along *ab* begins at least 20 °C higher than the transition along *c*;

however, this transition is not complete before doubling along the channel, which allows the possibility that these transitions may be correlated. The very large temperature range (ca. from -145 to -170 °C) over which expansion in along *a* and *b* occurs would make it difficult for a calorimetry experiment to detect such a transition if the enthalpy changes were small enough; this agrees with the lack of thermal behavior observed in DSC experiments. However, the sensitivity of X-ray diffraction is apparently great enough to observe this process. Upon further cooling, additional structural changes occur around -171 to -173 °C. These abrupt changes in intensity begin at -172 °C (*ab* plane, reflection ($\bar{1}$ 9 0)) and at -173 °C (*c* axis, reflection ($\bar{1}$ 7 $\bar{3}$)) and may correspond to the two thermal anomalies observed in DSC measurements (Figure 3.3).

An alternative explanation for the abrupt change in reflection intensity observed around -171 to -173 °C is hysteresis in the cooling transition caused by heating to -161 °C before recooling to -171 and -172 °C.[63] However, hysteresis appears unlikely because the crystal was held at each temperature for at least 30 minutes for image collection, and because the behavior of ($\bar{1}$ 9 0) and ($\bar{1}$ 7 $\bar{3}$) are divergent (especially between -171 and -172 °C).

To summarize the X-ray experiments and Figure 3.4, cooling from high temperatures (8 × 8 × 44 Å trigonal cell, Figure 3.4a) induces three phase transitions in a crystal of 2,9-decanedione/urea. Near -145 °C, additional reflections in *a*b** indicate the gradual emergence of a superstructure in which *a* and *b* are increased by factors of 2 and $2\sqrt{3}$, respectively.) This process appears to continue through the lowest temperatures studied (-183 °C), where reflections from this expanded cell are quite intense (Figure 3.4b). Further cooling (from -145 °C) induces two additional phase transitions, at least

one of which involves doubling along the channel (*c*) axis. At around -169 °C (Figure 3.4e), reflections from this cell are barely detectable; by -173 °C (Figure 3.4c), however, the cell is conspicuous. This process appears to follow structural rearrangement in the *ab* plane, as indicated by an increase in intensity for reflection ($\bar{1}$ 9 0) at -172 °C. Diffraction data collected on the low temperature phase demonstrates three unit cells of orthorhombic symmetry (or lower) that are distorted from hexagonal metric symmetry. In analogy to ferroelastic 2,10-undecanedione/urea, these cells (each related by ~60° rotation about the channel axis) were identified in the low temperature phase. The assignment of orthorhombic (or lower) metric symmetry agrees with the optical behavior of this phase, described below.

3.1.3 Crystal Optics

The optical behavior of the crystal at reduced temperatures can provide insight into the nature of the phase transitions as well as confirmation of the reduction in point symmetry suggested by the diffraction experiments. At room temperature, 2,9-decanedione/urea possesses $\bar{3}$m Laue symmetry; the coincidence of the optic axis with the channel axis makes these crystals optically uniaxial when viewed through the plate face.[64] (Refer to Section 1.1.2.) In the diffraction work described above, the low temperature phase appeared to exhibit orthorhombic (or lower) symmetry. This phase should therefore be easily observable because orthorhombic, monoclinic and triclinic crystals are optically biaxial; under the polarizing microscope, the cooled crystal should appear birefringent. An experiment designed to observe the optical properties of the low

temperature phase can therefore provide important information about this phase transition.

In this experiment, a crystal of 2,9-decanedione/urea was cooled to cryogenic temperatures under the polarizing microscope. For this experiment, the apparatus depicted in Figure 3.5 was constructed in collaboration with B. L. Champion.[65] This device was built around a cold stream apparatus previously used with a Weissenberg camera and the Nikon Microphot-SA polarizing microscope. For the cooling experiment, the crystal was mounted with epoxy adhesive to a glass pin. A microscope-mountable goniometer (built by the Charles Supper Co.) was used to hold and orient the crystal on the microscope. The combination of the goniometer and rotatable microscope stage allowed rotation along axes parallel and perpendicular to the microscope light path. (These rotations correspond to χ and ϕ on a four-circle diffractometer.) Cold gaseous helium was introduced from a liquid helium dewar via the Weissenberg cooler. The tip of this device has an inner diameter of approximately 5.5 mm, into which was inserted a Watlow 30 watt cartridge heater (ARS #C1EX68A); see E in Figure 3.5. In conjunction with a Lakeshore Cryotronics DRC-91C temperature controller, this heating element was used to control the rate of cooling. The crystal temperature was measured with a copper-constantan (0.005" diameter, Omega) thermocouple mounted at the nozzle output. The thermocouple was calibrated[66] by measuring the temperature of liquid nitrogen (-196.0 °C, corrected for barometric pressure[67]) and the melting points of ethanol, methanol and decane (m.p. -114.1, -97.8 and -29.7 °C, respectively[68]). Corrections for crystal distance were made by correlating the temperature output of this thermocouple with the output of a similarly calibrated silicon diode sensor set at the same relative position as the crystal in

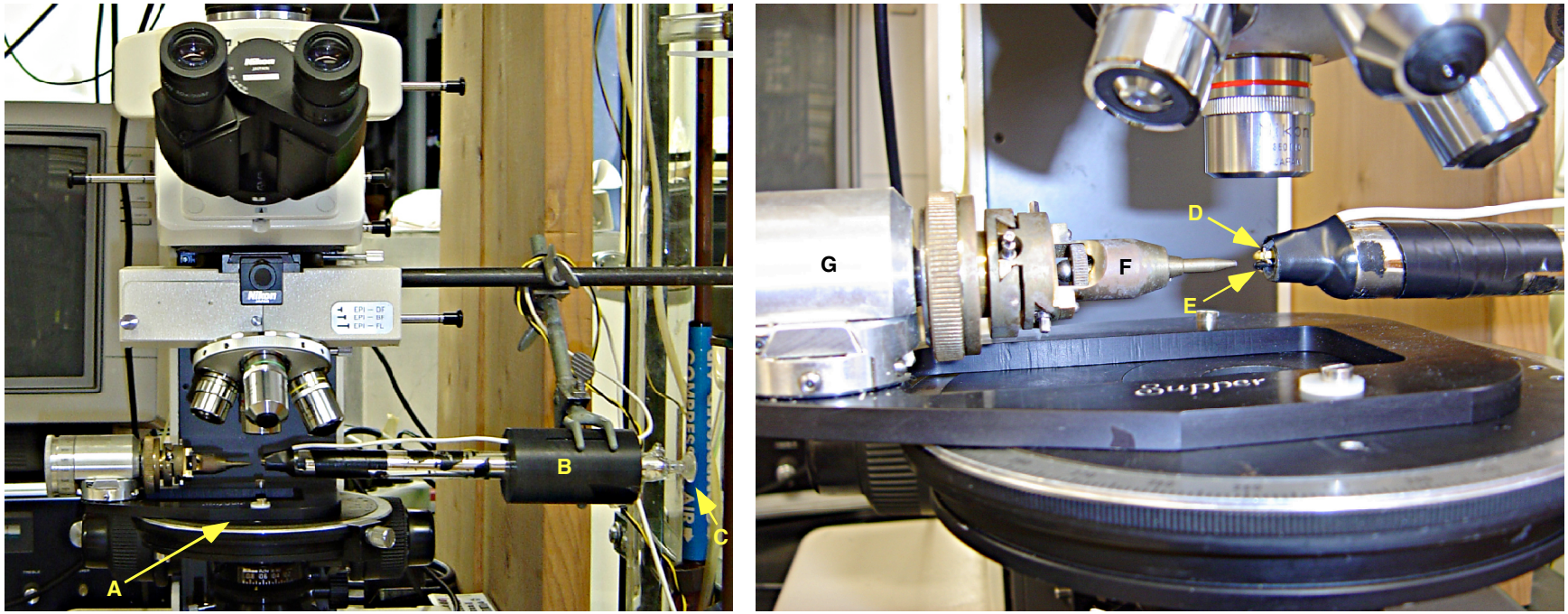

Figure 3.5 The apparatus used for the optical investigation of low temperature phase transitions in 2,9-decanedione/urea. (The crystal and phase transition are illustrated in Figures 3.6 and 3.7.) This device was attached to the stage (A) of a Nikon Microphot-SA microscope and utilized the cold stream apparatus from a Weissenberg camera (B). Cold helium gas was delivered to the device (C) from a pressurized liquid helium dewar (not shown). A copper-constantan thermocouple (0.005" diameter) inserted into the end of nozzle (D) measured the temperature of the outgoing gas, while a cartridge heater and temperature controller were used to regulate the temperature (see wires at E). Around the nozzle, an envelope of dry helium gas was provided by a ring of smaller nozzles (not shown); this served to enshroud the cold stream and reduce condensation on the crystal. The crystal was mounted on a goniometer head (F) which was held in place by a stage-mounted goniometer from Charles Supper Co. (G). The closest edge of the crystal was approximately 1.9 mm from the output of the cold nozzle. This goniometer and stage setup allowed the facile alignment and rotation of the crystal. For this experiment, this apparatus was surrounded by a large plastic bag (not shown) that was inflated to a positive pressure with gaseous helium. The positive helium pressure within this bag reduced the condensation of moisture and other atmospheric gases at very low temperatures.

the experiment. For this calibration the correlation of "crystal" temperature with "nozzle" temperature (spaced apart by approximately 1.9 mm) was linear over the range of calibration standards, with $R^2 = 0.996$.[66]

One final consideration was that the condensation or freezing of moisture (or other gases) present in the atmosphere might cloud visual observations (or destroy the crystal entirely). This problem was addressed in two ways. The cooling stream was enshrouded with dry helium supplied by seven tiny hoses fastened by a small nylon ring at the nozzle tip. The dry helium helped to separate the cold helium and the crystal from the atmosphere and reduce the condensation of other gases. In addition, the entire apparatus was sealed in a plastic glove bag pressurized with helium (from both the cold stream apparatus and the helium envelope nozzles). These measures minimized the effects of condensing vapors to temperatures approaching 10 K.

The low temperature experiment was performed on a UIC of 2,9-decanedione that had been grown by slowly cooling a methanol solution of 2 M urea and 2,9-decanedione (1:9 molar ratio). The crystal, shown in Figure 3.6a-c, demonstrates the uniaxial behavior anticipated from its trigonal symmetry. (Photomicrographs a-c were collected by B. L. Champion.) Furthermore, this crystal exhibits large chiral twins that are easily observed by slightly uncrossing the polarizers (Figure 3.6d-f). Boundaries separating chiral twins are thought to be composed of *stacked loop* urea channels.[69] The stacked loop is similar to its helical counterpart in that it forms a channel inside which linear guests reside; however, the glide symmetry exhibited by this topology is expected to inhibit domain wall motion for stacked loop UICs.[70] For this experiment it was considered plausible that they might impede a possible phase transition front so that

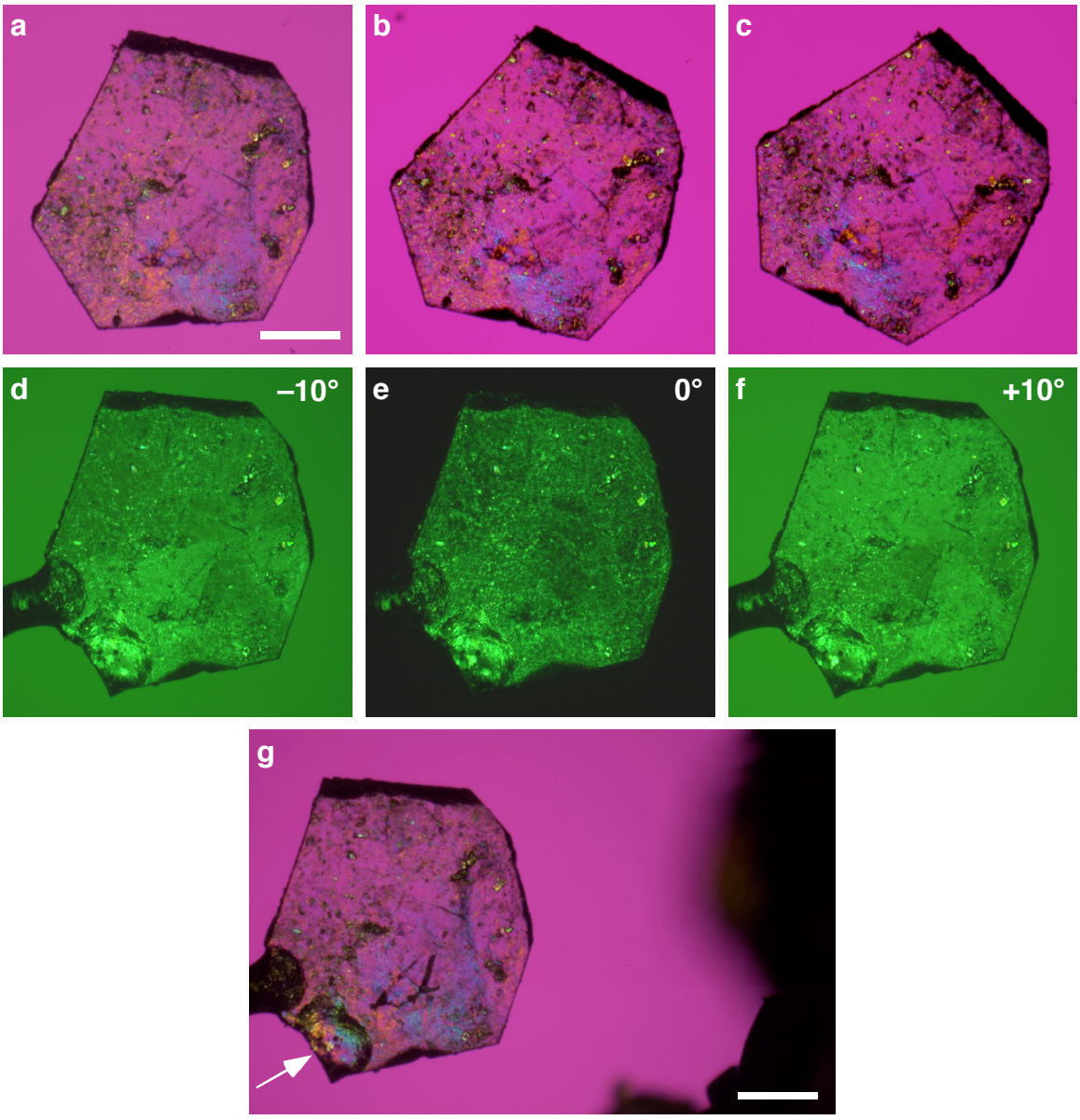

Figure 3.6 The crystal of 2,9-decanedione/urea used in cooling experiments, at room temperature. **(a-c)** Photomicrographs taken between crossed polars and with λ plate at 0°, 15° CW and 30° CW relative orientation illustrate the uniaxial optics observed for UICs of 2,9-decanedione. In these images and others (see Figure 3.7), birefringence is observed in the lower portion of the crystal; for this region the slow axis appears to rotate with the crystal. This may be due to poor condensation optics at 1.3x or from the crystal not setting perfectly flat on the microscope. Scale bar = 0.50 mm (Nikon 1.3x). **(d-f)** The crystal was mounted to a glass pin with a small amount of epoxy adhesive. (Some epoxy from a previous mounting attempt is visible towards the bottom – see arrow in **g**.) Here, the crystal is positioned on a stage-mounted goniometer. Photomicrographs, taken between nearly crossed polars and with green interference filter, demonstrate optical rotation from the chiral urea channels (see Section 2.3.3.3). **(d)** Analyzer rotated –10°. Here, dextrorotatory regions appear darker than they are in **e**. **(e)** Analyzer and polarizer crossed. **(f)** Analyzer rotated +10°. Here, levorotatory regions appear darker than they are in **e**. From these photos it is noted that the top portion of this crystal is a single dextrorotatory domain while the bottom portion is composed of three chiral twins. **(g)** The crystal with cooling nozzle in place. Here, wires and insulation of the cold stream apparatus are seen on the right. The crystal is estimated to be 1.9 mm from the cold stream output. Scale bar = 0.50 mm (Nikon 1.3x). Photos **a-c** recorded by B. L. Champion.

different twins could be observed on either side of the chiral twin boundary. However, as discussed below, chiral twin boundaries are not the only contributor to the domain structure of the low temperature phase.

In the experiment (performed in collaboration with B. L. Champion), the crystal was cooled to temperatures near -263 °C (10 K) three times; in each cycle the crystal exhibited biaxial crystal optics at temperatures below about -166 °C (97 K).[71] Such a change in optical symmetry supports the ferroelastic phase transition demonstrated in the diffraction experiments. A summary of the second trial is provided in Figure 3.7. (In the first trial, poor temperature control caused the phase transition to occur very rapidly so that this trial was not recorded with photomicrographs. Fortunately, video recordings of all three cooling runs demonstrate similar behavior for the crystal in each experiment. These images are not provided because the video[72] resolution is poor in comparison to the resolution afforded by still photomicrographs.) As it is cooled, the crystal shows the first signs of birefringence near -165.8 °C (Figure 3.7b). By -179 °C (Figure 3.7d), the entire crystal has undergone the phase transition. However, it must be emphasized that the temperature is known only for the leading edge of the crystal; in this flowing system, large thermal gradients are inevitable, so the far side of the crystal (which is approximately 3.5 mm from the cold stream nozzle) is thought to be at a significantly higher temperature. Thus, the apparently large range of temperature over which this phase transition occurs is probably overestimated.

In the low temperature phase (Figure 3.7c-f), the crystal is a cluster of birefringent twins. Rotational twinning was confirmed by rotating the microscope stage (Figure 3.7e). Here, the interference colors of some of these domains can be seen to change

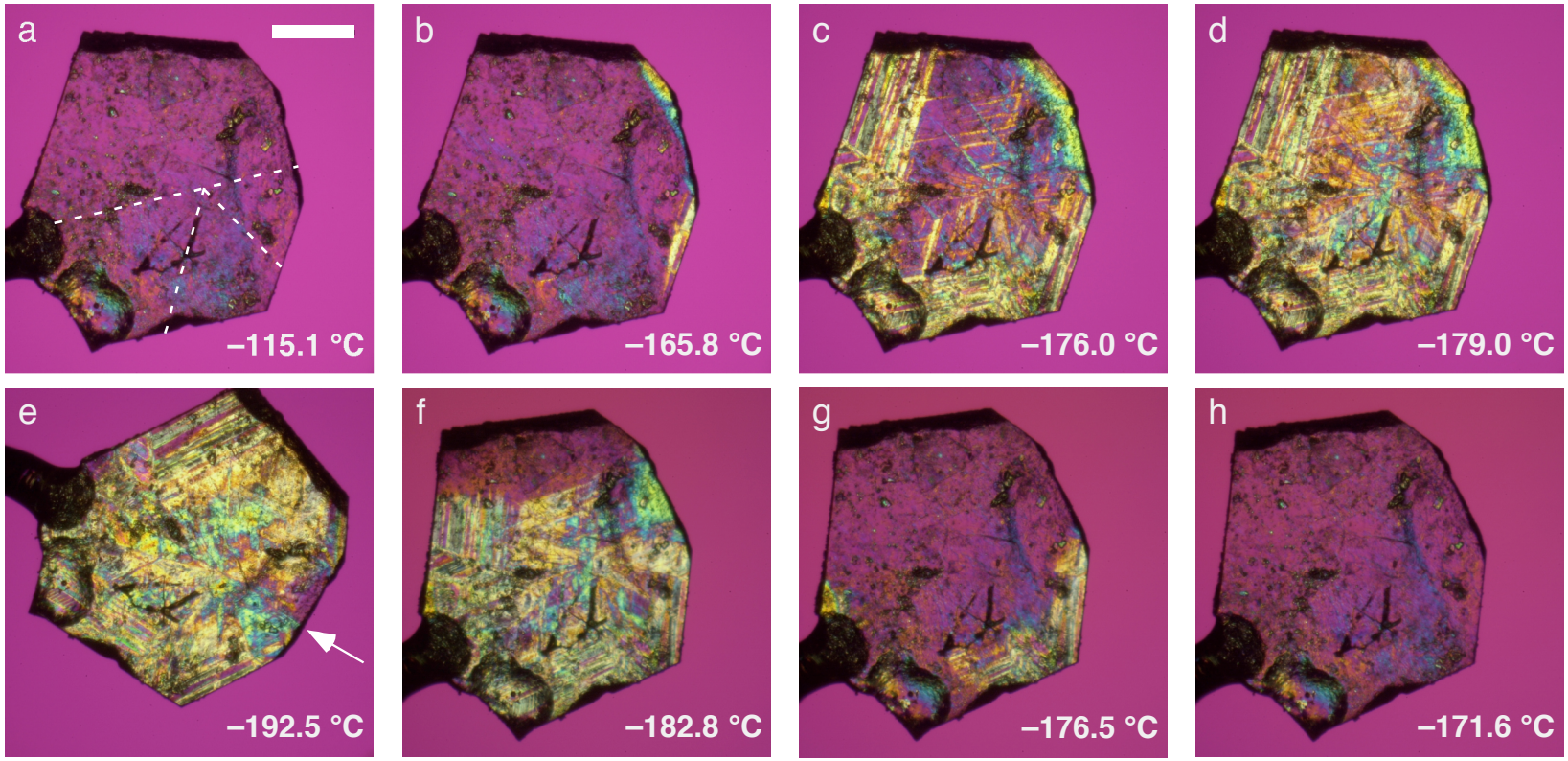

Figure 3.7 Optical photomicrographs of 2,9-decanedione/urea at low temperatures (crossed polars, λ plate). The cold nozzle (not shown) lies ~1.9 mm to the right of the crystal (Figure 3.6). **(a-e)** Cooling. **(a)** Above the phase transition. Here, the approximate positions of the chiral twin boundaries (Figure 3.6) are denoted by the dashed lines. Scale bar = 0.50 mm (Nikon 1.3x). **(b)** The phase transition is first observable at –165.8 °C and continues to around –179 °C (over a span of about 1.5 minutes). **(d)**. By –179 °C the phase transition appears complete, and the crystal is composed of many biaxial domains. In **e** the crystal was rotated 34° clockwise to demonstrate different slow axis orientations for different domains. The arrows indicate the location of chiral twin boundaries (as in **a**). **(f-h)** Warming; in this image the crystal has been rotated 12° counterclockwise from **a**. At this point, the crystal has been in the low temperature phase for approximately 58 minutes. The transition to the high-temperature phase is complete by –171.6 °C (**h**). For this experiment, temperature measurement was performed using a thermocouple located at the cold nozzle; the temperatures shown were adjusted to compensate for the distance separating the nozzle and leading edge of the crystal. Nevertheless, these temperatures may not be reliable to better than 5 °C ($T_{crystal} \geq T_{nozzle}$).

while other domains become extinguished. The formation of multiple domains is to be expected in ferroelastic phase transitions in which the crystal is not secured in a way that favors formation one orientation state over the others. In practice, the formation of one ferroelastic orientation state at the expense of the others can be induced by clamping, whereas ferroelectrics can be poled[73] in a fashion to provide a single domain orientation. In the present case, no such steps were taken, and the low temperature phase is free to exhibit a rich domain structure. As discussed above, these twins should occur in three orientations, as specified by the 32F2 ferroelastic species.

Inspection of the photomicrographs taken of the low temperature phase suggests chiral twin boundaries may serve as domain boundaries in the twinned crystal at low temperatures. The approximate locations of these boundaries are outlined in Figure 3.7a, according to their positions provided in Figure 3.6d-f. Throughout the series of photomicrographs, the perceived domain "texture" of the crystal appears to change abruptly in the locations where chiral twinning occurs. This effect is especially pronounced in photomicrograph Figure 3.7e (see arrow). For this image the crystal was rotated (34° CW) so that the domain on one side of the chiral boundary is extinguished while the other is not. These rotational twins appear to be separated by the chiral twin boundary. (Note similar optical behavior for this region in Figure 3.7c and d.)

Although it is tempting to attribute the changes in domain structure to the chiral twin boundaries, 60° rotational (Dauphiné) twinning quite often accompanies chiral twinning in nominally trigonal systems such as 2,12-tridecanedione/urea,[69] and mixed UIC crystals of 2,9-decanedione and 2-decanone.[74] While such rotational twin boundaries are not visible in optical photomicrographs, rotational twinning along this

chiral twin boundary can easily account for the generation of domains that are related by the same 60° rotation. Certainly, the presence of Dauphiné twins can predispose this crystal to form multiple domains in the low temperature phase since a cooperative layer-by-layer transformation would naturally lead to rotational twins. Thus, the rich domain structure exhibited by this crystal appears to be influenced by rotational twinning, and possibly by chiral twinning. In addition, artificial perturbations such as uneven cooling, crystal history and rigidity caused by the epoxy resin used to mount the crystal (one sort of "clamping") could bias the growth of domain structure of the low temperature phase.

3.2 Discussion

The low temperature phase transition observed in 2,9-decanedione/urea is ferroelastic because it involves a change in optical symmetry, which implies a change in point group. X-ray diffraction experiments demonstrate a distorted unit cell in this phase that possesses orthorhombic or lower symmetry. In his discussion[14] of ferroelastic phase transitions, Aizu also identified a phase transition to triclinic symmetry (32F1). Although the present work does not distinguish between these alternatives, it may be possible to determine the Laue symmetry of the low temperature phase by a thorough examination of reflection intensities. Regardless, it can be concluded that unit cell distortion accompanies this phase transition; it is therefore a *proper ferroelastic phase transition*.[75]

In X-ray oscillation images collected during the phase transition, one notes the emergence of diffuse scattering along c^* (Section 3.1.2.) At -145 °C (see Figure 3.4f) the superstructure layers are composed of diffuse bands; the intensity of these bands is reduced at lower temperatures as discrete reflections gradually emerge. The orientation

of the diffuse bands (along c^*) suggests that the correlation length along the channel axis is too small to provide sharp diffraction maxima. Analogously, the relatively well-defined layer positions along a^*b^* suggest a greater correlation length perpendicular to the channel. These observations provide clues to a possible mechanism for the phase transition, in which ordering in the ab plane occurs in layers that are oriented perpendicular to the channel. As more of these layers become ordered, ordering along c^* is apparently increased, the enlarged unit cell becomes detectable, and the crystal exhibits biaxial optical behavior.

The potential for ferroelasticity in trigonal UICs based on 2,9-decanedione presents an interesting comparison to the digonal UICs containing 2,10-undecanedione. Although divergent in aspects such as crystal symmetry and ferroelastic properties, these crystals exhibit many structural similarities, including their commensurate structures and the tendency to form host-guest hydrogen bonds. The importance of interactions between host and guest cannot be overlooked; as demonstrated in Chapters 4 and 5, such interactions are critical to the ferroelastic properties of 2,10-undecanedione/urea and related crystals.

References Cited

1. Lines, M. E. & Glass, A. M. *Principles and Applications of Ferroelectrics and Related Materials*, (Clarendon Press, Oxford, 1977), pp. 24-58.
2. Wadhawan, V. K. *Introduction to Ferroic Materials*, (Gordon and Breach Science Publishers, Amsterdam, 2000), pp. 123-188.
3. Wadhawan, V. K. Ferroelasticity: introductory survey and present status. *Phase Transit.* **34**, 3-18 (1991).
4. Wadhawan, V. K. & Glazer, A. M. Prototype symmetry of the ferroelastic superconductor Y-Ba-Cu-O. *Phys. Rev. B* **39**, 9631-9632 (1989).
5. Wadhawan, V. K., Somayazulu, M. S. & Sastry, P. U. M. Assignment of prototype symmetry for the Y-Ba-Cu-O superconductor and some predictions based on this assignment. *Phys. Rev. B* **38**, 2509-2512 (1988).
6. Camps, R. A., Evetts, J. E., Glowacki, B. A., Newcomb, S. B., Somekh, R. E. & Stobbs, W. M. Microstructure and critical current of superconducting $YBa_2Cu_3O_{7-x}$. *Nature (London)* **329**, 229-232 (1987).
7. Gregoryanz, E., Hemley, R. J., Mao, H.-K. & Gillet, P. High-pressure elasiticy of α-quartz: Instability and ferroelastic transition. *Phys. Rev. Lett.* **84**, 3117-3120 (2000).
8. Valasek, J. Piezo-electric and allied phenomena in rochelle salt. *Phys. Rev.* **17**, 475-481 (1921).
9. Megaw, H. D. *Ferroelectricity in Crystals*, (Methuen & Co Ltd, London, 1957), pp. 14-15.
10. Solans, X., Gonzalez-Silgo, C. & Ruiz-Perez, C. A structural study on the rochelle salt. *J. Solid State Chem.* **131**, 350-357 (1997).
11. Tsukamoto, T., Hatano, J. & Futama, H. Refraction and reflection of light at ferroelastic domain walls in rochelle salt crystal. *J. Phys. Soc. Japan* **51**, 3948-3952 (1982).
12. Toledano, P. & Toledano, J.-C. Nonferroic phase transitions. *Phys. Rev. B* **25**, 1946-1964 (1982).
13. Mackenzie, G. A., Arthur, J. W. & Pawley, G. S. The structural phase transition in octafluoronaphthalene. *J. Phys. C: Solid State* **10**, 1133-1149 (1977).
14. Aizu, K. Possible species of "ferroelastic" crystals and of simultaneously ferroelectric and ferroelastic crystals. *J. Phys. Soc. Japan* **27**, 387-96 (1969).
15. Aizu, K. The concepts "prototype" and "prototypic phase" – Their difference and others. *J. Phys. Soc. Japan* **44**, 683 (1978).
16. Aizu, K. Possible species of ferromagnetic, ferroelectric, and ferroelastic crystals. *Phys. Rev. B* **2**, 754-772 (1970).
17. Aizu, K. Determination of the state parameters and formulation of spontaneous strain for ferroelastics. *J. Phys. Soc. Japan* **28**, 706-16 (1970).
18. Hollingsworth, M. D. & Harris, K. D. M. "Urea, Thiourea, and Selenourea" in *Comprehensive Supramolecular Chemistry*, vol. 6 (eds. MacNicol, D. D., Toda, F. & Bishop, R.) (Pergamon Press, New York, 1996) pp. 177-237.

19. Forst, R., Boysen, H., Frey, F., Jagodzinski, H. & Zeyen, C. Phase transitions and ordering in urea inclusion compounds with *n*-paraffins. *J. Phys. Chem. Solids* **47**, 1089-97 (1986).
20. Lauritzen, J. I., Jr. Analysis of dielectric loss in two urea addition compounds: the hindered single-axis polar rotator. *J. Chem. Phys.* **28**, 118-31 (1958).
21. McAdie, H. G. Thermal decomposition of molecular complexes. III. Urea inclusion compounds of monosubstituted aliphatic series. *Can. J. Chem.* **41**, 2144-2152 (1963).
22. McAdie, H. G. Thermal decomposition of molecular complexes. I. Urea-*n*-paraffin inclusion compounds. *Can. J. Chem.* **40**, 2195-2203 (1962).
23. White, M. A. & Harnish, R. S. Thermodynamic studies of two different inclusion compounds with the same guest: Toward a general understanding of melting behavior in binary compounds. *Chem. Mater.* **10**, 833-839 (1998).
24. Chatani, Y., Taki, Y. & Tadokoro, H. Low-temperature form of urea adducts with *n*-paraffins. *Acta Crystallogr. B* **33** (1977).
25. Chatani, Y., Anraku, H. & Taki, Y. Phase transition and structure change of urea adducts with *n*-paraffins and paraffin-type compounds. *Mol. Cryst. Liq. Cryst.* **48**, 219-231 (1978).
26. Forst, R., Jagodzinski, H., Boysen, H. & Frey, F. Diffuse scattering and disorder in urea inclusion compounds $OC(NH_2)_2 + C_nH_{2n+2}$. *Acta Crystallogr. B* **43**, 187-97 (1987).
27. Guillaume, F., Sourisseau, C. & Dianoux, A. J. Inelastic incoherent neutron scattering study of molecular motions of *n*-nonadecane in urea clathrate. *J. Chem. Phys.* **93**, 3536-41 (1990).
28. Le Lann, H., Odin, C., Toudic, B., Ameline, J. C., Gallier, J., Guillaume, F. & Breczewski, T. Single-crystal deuterium NMR study of the symmetry breaking in an incommensurate organic inclusion compound. *Phys. Rev. B* **62**, 5442-5451 (2000).
29. Rubio-Peña, L., Breczewski, T. & Bocanegra, E. H. Ferroelastic phase transition in the urea inclusion compounds: *n*-Heptadecane/urea and *n*-nonadecane/urea. *Ferroelectrics* **269**, 171-176 (2002).
30. Parsonage, N. G. & Pemberton, R. C. Thermodynamic properties of urea-hydrocarbon adducts. Part 2. *Trans. Faraday Soc.* **62**, 553-557 (1966).
31. Parsonage, N. G. & Pemberton, R. C. Thermodynamic properties of urea-hydrocarbon adducts. Part 1. *Trans. Faraday Soc.* **61**, 2112-2121 (1965).
32. Parsonage, N. G. & Pemberton, R. C. Thermal anomalies in the adducts of urea with *n*-paraffins. *Trans. Faraday Soc.* **63**, 311-328 (1967).
33. Hollingsworth, M. D. Personal communication to J. R. Rush (2005).
34. Fukao, K. X-ray scattering and disordered structure of *n*-tetracosane in urea adducts. I. A model for the x-ray scattering pattern. *J. Chem. Phys.* **101**, 7882-92 (1994).
35. Fukao, K. X-ray scattering and disordered structure of *n*-tetracosane in urea adducts. II. Averaged disorder, spatial correlation, and phase transition. *J. Chem. Phys.* **101**, 7893-903 (1994).

36. Guillaume, F., Sourisseau, C. & Dianoux, A. J. Rotational and translational motions of *n*-nonadecane in the urea inclusion compound as evidenced by incoherent quasielastic neutron scattering. *J. Chim. Phys. PCB*. **88**, 1721-39 (1991).
37. Welberry, T. R. & Mayo, S. C. Diffuse X-ray scattering and Monte-Carlo study of guest-host interactions in urea inclusion compounds. *J. Appl. Crystallogr.* **29**, 353-364 (1996).
38. Rubio-Peña, L., Breczewski, T., Bocanegra, E. H. & Madariaga, M. Ferroelastic phase transition and domain structure in urea inclusion compounds with two different guest families: *n*-alkanes and α,ω-dicarboxylic acids. *Ferroelectrics* **290**, 177-185 (2003).
39. Hollingsworth, M. D., Bacsa, J., Campana, C. F. & Peterson, M. L. "Translational disorder and crystal growth mechanisms in channel inclusion compounds," presented at the American Crystallographic Association National Meeting, Chicago, IL. (2004).
40. Brown, M. E. & Hollingsworth, M. D. Stress-induced domain reorientation in urea inclusion compounds. *Nature (London)* **376**, 323-7 (1995).
41. Hollingsworth, M. D., Brown, M. E., Hillier, A. C., Santarsiero, B. D. & Chaney, J. D. Superstructure control in the crystal growth and ordering of urea inclusion compounds. *Science (Washington, D. C.)* **273**, 1355-1359 (1996).
42. Rush, J. R. Laboratory notebook entry jrr-e263. See jrr-e263.xls. (2005).
43. Gilson, F. R. & McDowell, C. A. Nuclear magnetic resonance studies of urea and thiourea adducts. *Mol. Phys.* **4**, 125-134 (1961).
44. Weber, T., Boysen, H. & Frey, F. Longitudinal positional ordering of *n*-alkane molecules in urea inclusion compounds. *Acta Crystallogr. B* **56**, 132-141 (2000).
45. Harris, K. D. M. & Thomas, J. M. Structural aspects of urea inclusion compounds and their investigation by X-ray diffraction: a general discussion. *J. Chem. Soc., Faraday Trans.* **86**, 2985-96 (1990).
46. Rabiller, P., Etrillard, J., Toupet, L., Kiat, J. M., Launois, P., Petricek, V. & Breczewski, T. Disorder versus structure analysis in intergrowth urea inclusion compounds. *J. Phys. Condens. Mat.* **13**, 1653-1668 (2001).
47. Hollingsworth, M. D. Laboratory notebook entry mdh-n-221-11. (2005).
48. Rush, J. R. Laboratory notebook entry jrr-f094-3. (2006).
49. Rush, J. R. Laboratory notebook entry jrr-f094-5. (2006).
50. Hollingsworth, M. D. Laboratory notebook entry mdh-n-223-24. (2005).
51. Rush, J. R. Laboratory notebook entry jrr-f270-5. (2007).
52. Rush, J. R. Laboratory notebook entry jrr-f270-8. (2007).
53. Rush, J. R. Laboratory notebook entry jrr-f270-6. (2007).
54. Rush, J. R. Laboratory notebook entry jrr-f091. (2006).
55. Hollingsworth, M. D. Personal communication to J. R. Rush (2007).
56. Rush, J. R. Laboratory notebook entry jrr-f284. See also entries jrr-f268 and jrr-f273. (2007).

57. Catti, M. & Ferraris, G. Twinning by merohedry and X-ray crystal structure determination. *Acta Crystallogr. A* **32** (1976).
58. Cahn, R. W. Twinned crystals. *Adv. Phys.* **3**, 363-445 (1954).
59. Rush, J. R. Laboratory notebook entry jrr-f092-7. (2006).
60. Rush, J. R. Laboratory notebook entry jrr-f092-4. (2006).
61. Rush, J. R. Laboratory notebook entry jrr-f272. (2007).
62. Rush, J. R. The analysis of reflections (`1 9 0) and (`1 7 `3) is described in laboratory notebook entries jrr-f266 and f267 (region m) and jrr-f271 (region o), respectively. (2007).
63. Hollingsworth, M. D. Laboratory notebook entries mdh-n-224-30 through mdh-n-225-40. (2005).
64. Wood, E. A. *Crystals and Light*, (Dover Publications, Inc., New York, 1977), pp. 79-93.
65. Rush, J. R., Champion, B. L. & Hollingsworth, M. D. Laboratory notebook entry jrr-a276. (2003).
66. Rush, J. R. & Champion, B. L. Laboratory notebook entry jrr-a289. The associated electronic files are located in the folder for Figure 3.5. (2003).
67. Hollingsworth, M. D. Correlation of liquid nitrogen boiling point with barometric pressure. *Laboratory notebook entry DRC-91C*, 11-15 (1989).
68. Weast, R. C. (ed.) *CRC Handbook of Chemistry and Physics, 54th Edition* (CRC Press, Cleveland, 1973).
69. Hollingsworth, M. D., Brown, M. E., Dudley, M., Chung, H., Peterson, M. L. & Hillier, A. C. Template effects, asymmetry, and twinning in helical inclusion compounds. *Angew. Chem. Int. Ed.* **41**, 965-969 (2002).
70. Hollingsworth, M. D., Peterson, M. L., Pate, K. L., Dinkelmeyer, B. D. & Brown, M. E. Unanticipated guest motion during a phase transition in a ferroelastic inclusion compound. *J. Am. Chem. Soc* **124**, 2094-2095 (2002).
71. Rush, J. R. & Champion, B. L. Laboratory notebook entries jrr-a293 and jrr-a294. (2003).
72. Rush, J. R. DVD video: jrr-a292 (on two discs), recorded March 4, 2003.
73. Scott, J. F. *Ferroelectric Memories*, (Stringer-Verlag, London, 2000), pp. 2–7.
74. Hollingsworth, M. D. & Raghothamachar, B. Laboratory notebook entry mdh-m-111-4. (2002).
75. Wadhawan, V. K. Ferroelastic phase transitions. *Mater. Sci. Forum* **3**, 91-110 (1985).